Understanding progressive failure mechanisms of a wind turbine blade trailing edge section through subcomponent tests and nonlinear FE analysis

Chen, Xiao; Berring, Peter; Madsen, Steen Hjelm; Branner, Kim; Semenov, Sergei

Published in:
Composite Structures

Link to article, DOI:
10.1016/j.compstruct.2019.02.024

Publication date:
2019

Document Version
Peer reviewed version

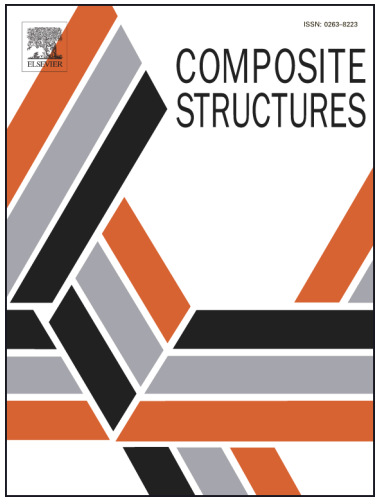

Understanding progressive failure mechanisms of a wind turbine blade trailing edge section through subcomponent tests and nonlinear FE analysis

Xiao Chen, Peter Berring, Steen Hjelm Madsen, Kim Branner, Sergei Semenov

PII: S0263-8223(18)33390-7
DOI: https://doi.org/10.1016/j.compstruct.2019.02.024
Reference: COST 10649

To appear in: *Composite Structures*

Received Date: 23 September 2018
Revised Date: 16 January 2019
Accepted Date: 7 February 2019

Please cite this article as: Chen, X., Berring, P., Madsen, S.H., Branner, K., Semenov, S., Understanding progressive failure mechanisms of a wind turbine blade trailing edge section through subcomponent tests and nonlinear FE analysis, *Composite Structures* (2019), doi: https://doi.org/10.1016/j.compstruct.2019.02.024

Understanding progressive failure mechanisms of a wind turbine blade trailing edge section through subcomponent tests and nonlinear FE analysis

Xiao Chen*, Peter Berring, Steen Hjelm Madsen, Kim Branner*, Sergei Semenov

Technical University of Denmark, Department of Wind Energy
Frederiksborgvej 399, 4000 Roskilde, Denmark

Corresponding authors:
Xiao Chen xiac@dtu.dk
Kim Branner kibr@dtu.dk

Abstract:

This paper presents a comprehensive study on structural failure of a trailing edge section cut from a composite wind turbine blade. The focus is placed on understanding progressive failure behavior of the trailing edge section in subcomponent testing during its entire failure sequence. Digital Image Correlation (DIC) is used to capture buckling deformation and strain distributions of the specimen. Detailed post-test inspection is performed to identify failure modes and failure characteristics. A nonlinear Finite Element (FE) model that accounts for all observed failure modes is developed based on continuum damage mechanics and progressive failure analysis techniques. Multiple structural nonlinearities originate from buckling, and contact and material failures are included in the model to predict the failure process. The study shows that in addition to the buckling-driven failure phenomenon, the surface contact of sandwich panels contributes to the failure process of the trailing edge section. Foam materials start to fail before the ultimate load-carrying capacity of the specimen is reached, while both composite materials and adhesive materials fail in the post-peak regime. The matrix-dominant failure and delamination develop before the fiber-dominant failure in composite laminates. The proposed FE model captures the progressive failure process of the trailing edge section reasonably well.

Keywords:

Buckling; delamination; composite failure; debonding; Digital Image Correlation (DIC); progressive failure analysis

1. Introduction

Trailing edge failure is one of the common structural failures of composite wind turbine blades. Extensive experimental investigations and numerical studies have been carried out in previous work [1-5] to understand failure behavior of trailing edges in the full-scale blades. It is now well known that the failure of the trailing edge under ultimate static loading is primarily buckling-driven. Typical failure modes observed in full-scale blade tests includes adhesive joint debonding, sandwich core failure and composite laminate failure. In recent years, subcomponent testing has been used [6-10] to understand the structural behavior of critical parts of composite blades. The subcomponent testing could be an important complement to the full-scale blade tests that are mandatory for certification of wind turbine blades. Regarding the subcomponents of trailing edges, efforts have been made to elaborate benefits of subcomponent over full-scale testing [8] and comparing different subcomponent test concepts [9]. Recent work [11] has assessed the failure of trailing edge subcomponents by addressing structural instability associated with pre-buckling and post-buckling response. The subcomponent tests offer a new opportunity to evaluate structural integrity of trailing edge sections, or any other critical parts, of composite rotor blades in more details. The trend of using subcomponent testing is also reflected by the 2015 DNV GL rotor blade standard DNVGL-ST-0376 [12], which makes it possible to use subcomponent testing as part of a blade certification [13].

The aforementioned studies [8-11] provide valuable knowledge on the structural response of trailing edge sections in the subcomponent tests. Nevertheless, two important questions remain. The first question is what is the entire failure sequence of a trailing edge section loaded to the final failure? It is known that the failure is often buckling-driven and that the buckling response in the pre-peak regime has been the primary focus in the existing studies. To a large extent, the buckling response determines the peak load, or the maximum load-carrying capacity, of the trailing edge sections. As another important part of the entire failure sequence, the post-peak response beyond the peak load has received far less attention. Typically, only experimental observations on failure modes after the tests are discussed, but how damages evolve in the post-peak regime is not fully understood. In the post-peak regime, material damages are generally more significant than in the pre-peak regime due to much larger deformation in the specimens and thus higher strains before their final failure. The post-peak response directly leads to the final failure modes and failure characteristics observed after the tests. It is of interest to investigate the post-peak response of trailing edge sections in order to have complete understanding of the entire failure sequence and the underlying failure mechanisms.

The second question is how to predict the failure sequence and failure modes of trailing edge sections? Predicting the failure of composite structures is a challenging task. Multiple structural nonlinearities are typically present and they include geometric nonlinearity, material nonlinearity and contact nonlinearity due to the change of boundary and load conditions. Existing studies use FE models, which are primarily based on shell elements together with certain failure criterion of composite materials, to predict stress/strain distribution and buckling response. When it comes to predicting the progressive failure sequence and the final failure modes of trailing edge sections, and so far, no public study has been able to predict these highly nonlinear structural behaviors accurately to the authors' best understanding. All three aforementioned types of structural nonlinearities have to be captured in order to provide accurate numerical predictions.

This study aims at providing possible answers to these two questions through comprehensive experimental investigation and advanced FE simulations. Three major research elements are included in the study:

(1) Detailed experimental investigation of trailing edge sections in subcomponent tests focusing on structural behavior including buckling, material damages and failure modes. Digital Image Correlation (DIC) is used to capture field variables, i.e., deformation and strains, of the trailing edge section during the entire failure sequence. Buckling and post-buckling responses are presented together with longitudinal and transverse strain distributions, providing direct experimental evidences of the final failure modes and failure characteristics that are identified through detailed post-test failure inspection.

(2) Development of a generic FE modeling technique capable of capturing the entire failure sequence that leads to the final failure characteristics. Three types of structural nonlinearities are taken into account in the FE model. Particular attentions are paid to modeling:

- Three-dimensional stresses/strains that are essential for accurate failure prediction of trailing edge sections. Geometric features of the test specimen are modeled using brick-like solid elements. Several layers of solid elements are used along the thickness direction of the trailing edge panels to better capture through-thickness stress/strain components in both sandwich skin laminates and foam core materials. The presented solid element model is much more detailed than the shell element models that have been used in other studies [1,3,5,9,11].
- Boundary and load conditions that represent the test setup as close as possible. Plywood and overlamination reinforcing the specimen boundaries are also included in the model. Sliding and pressing between two inside surfaces of sandwich panels are modeled to capture their contact status and possible effects on the structural response. Connector elements, rigid connections and Multiple Point Constraints (MPC) are used to model the load transfer system in the test.
- Multiple material damages that include composite material failure, foam core failure and adhesive failure. Continuum damage mechanics and progressive failure analysis techniques are used in the numerical analysis. Degradation of material properties are implemented so that local stresses around damages can be redistributed after material failure, allowing the progressive failure sequence of trailing edge sections to be captured accurately.

(3) Prediction of structural response and failure process of trailing edge sections observed in the experiment. Extensive comparisons between numerical predictions and experimental results are made with respect to buckling deformation, strain distributions, failure modes and failure characteristics. Numerical simulations complement experimental findings to obtain complete understanding of progressive failure mechanisms of trailing edge sections.

As such, this study aims to unveil the entire failure sequence of trailing edge sections taking into account multiple structural nonlinearities associated with buckling deformation, contact conditions and progressive damages of different materials. This is the first-of-its-kind study particularly focusing on the failure of trailing edge sections to the best of our knowledge. In addition, the FE model presented in this study is more detailed and accurate in predicting the failure sequence and multiple failure modes of trailing edge sections comparing to existing studies [9,11].

The following Section 2 describes the experimental setup used for testing a subcomponent of a trailing edge section. Test results and discussion are presented in Section 3. The development of the FE modeling method is presented in Section 4. In Section 5, numerical predictions are compared with experimental results. Based on these findings, Section 6 presents the failure mechanisms of trailing edge sections. Section 7 summarizes major conclusions of this study.

2. Experimental setup

2.1 Trailing edge section

In this study, the trailing edge section used in subcomponent test was cut from a 34m full-scale blade. The blade was first cut at two span-wise locations at 19.15 m and 22.15 m from the blade root, resulting in a 3m long blade section. Subsequently, the blade section was cut along a line where the in-plane normal strain values were zero in the edgewise loading configuration, see Figure 1. It is noted that the line through the cross section where the normal strain is zero is not necessarily aligned with the principal bending axis as the location of this line depends on the loading configuration. The cutting along this line was performed to reduce the required loading while still mimicking the edgewise loading, by applying a similar in-plane normal strain field, as the section would be exposed to in the full-scale blade.

The zero-strain axis was determined by a FE analysis where the full-scale blade is in the linear structural response regime under edgewise bending, i.e., the leading towards trailing edge loading case. Further loading will lead to trailing edge buckling of the blade. Figure 2 shows the buckling deformation of the blade when it is loaded under edgewise bending. The subcomponent specimen only has trailing edge panels in the compressive strain regime determined by the cutline as shown in Figure 1. More details on the full-scale blade and subcomponent specimen can be found in [14].

Figure 1. The subcomponent of a trailing edge section used in this study

Figure 2. Trailing edge buckling of a full-scale blade under edgewise bending

2.2 Test rig and boundary conditions

A U-shape test rig as shown in Figure 3(a) was developed to compress the trailing edge section to reproduce its structural response as close as possible to the one that the subcomponent would exhibit if it was situated in the full blade. The distance between two hinges is 3000 mm and the height of rotating arms is 1900 mm. As this study focuses on the structural failure of the trailing edge section in subcomponent test, great efforts have been made to avoid undesired premature failure at the specimen's boundaries. The hollow cross sections at both ends of the specimen, as shown in Figure 1, are reinforced internally by gluing in a layer of plywood with a thickness of approximately 21 mm using Spabond 340LV HT Epoxy adehsive. The specimen is then glued to the steel plates of the test rig. Further, two 21 mm layers of plywood are applied externally to clamp the specimen to the test rig. The Spabond 340LV HT Epoxy adhesive is also used to fill the gaps between the specimen and the plywood clamp. The epoxy adhesive was cured at 70 °C for 5 hours using heating pads after a night at room temperature. Overlamination using wet hand lay-up is applied to reinforce local materials near the clamped boundaries. At each boundary the area closest to the trailing edge are overlaminated 500 mm chordwise and 300 mm lengthwise using 7 layers of 450 g/m^2 biaxial glass fiber fabric in a West System 105 Epoxy resin, which cures at room temperature.

2.3 Instrumentation

A hydraulic actuator with a loading capacity of 500kN is used to load the trailing edge section under compression. The actuator is controlled by an Instron 8500 controller. The load is applied quasi-statically under displacement control with 0.1 mm/sec rate until the collapse of the specimen. The applied load is measured by a Honeywell Model 3156 load cell (±0.2% full scale non-linearity, ±0.2% full scale of hysteresis and ±0.05% full scale repeatability). The maximum load was within 60% of the load cell capacity. The displacement of actuator piston is measured by a Linear Variable Differential Transformer (LVDT). Both measurements are recorded by the controller with a 10 point/sec sampling rate.

Randomly distributed speckles with a diameter ranging approximately from 5 to 7mm are painted on the pressure side of the specimen for Digital Image Correlation (DIC) measurements as shown in Figure 3(b). The distance between speckles is around 7 mm. The GOM ARAMIS system with two 12 megapixel cameras are used to perform DIC measurements. Two cameras are fixed on a carbon fiber composite tube with a 1.6m length. The distance from the DIC system to the specimen is about 3.2m and the field of view is about 3x2m. The calibration is performed before the test following the standard procedure specified by the equipment producer. A 2m carbon fiber cross is used in the calibration procedure. The calibration error is within 0.09 pixel. During the test, the DIC measurements are recorded with a 2 frame/sec (FPS) rate and they are synchronized with applied load through analog force and displacement signals.

Figure 3. Subcomponent test setup

3. Test results and discussion

3.1 Displacement and strain response

The global structural response of the subcomponent specimen in terms of applied loads and actuator displacement is shown in Figure 4. The applied load is normalized by the peak load P_{peak} = 99.2 kN and the displacement is normalized by the total length of the specimen l_0 = 3 m. It can be seen that the specimen responds to the applied load in an approximately linear manner up to 80% P_{peak}, after which the slope of the applied load-displacement curve decreases, indicating the overall stiffness of the specimen is reduced. After the peak load at 100%P_{peak}, there is a smooth post-peak response followed by three significant drops of the load-carrying capacity occurred at 96%, 83% and 47% $P_{peak(post)}$, respectively.

Figure 4. The global structural response of the trailing edge section

The displacements measured by DIC provide more insight into the structural response. Figure 5 shows the out-of-plane deformation of the trailing edge section at eight load levels during the test. The contours show the displacement field of the blade specimen at the pressure side. In the contours, the positive values shown in red indicate the in-ward deformation, or the deformation toward the suction side of the specimen, whereas the negative values shown in blue indicate the out-ward deformation, or the deformation further away from the suction side of the specimen. In the figures, the out-of-plane displacement along two lines are also presented. One line is approximately 60 mm from the trailing edge and it is indicated as TE, and the other line is at the span-wise location and it is indicated as Section 21.45 m. The deformations along these two lines during the test are also plotted in the figures.

Figure 5. The out-of-plane deformation of the trailing edge section measured by DIC

It can be seen that the buckling deformation is well developed along the trailing edge and in the sandwich panel at 80% P_{peak}. Most of the specimen is a sandwich panel as it is between the trailing edge and the cutline, see Figure 1. At the 21.45 m section, the trailing edge buckles towards the pressure side while the sandwich panel buckles towards the suction side. The buckling deformation becomes significant with the applied loads. After the peak load 100% P_{peak}, debonding of adhesive joint occurs in the trailing edge at approximately the 21.60 m section at 47% $P_{peak(post)}$. The displacement curve at the trailing edge line (TE) also shows a noticeable change in shape comparing to the previous load level at 83% $P_{peak(post)}$. This is reasonable considering the change of the load transfer path due to the separation of the trailing edge bond line. The applied load drops dramatically from 83% to 47% $P_{peak(post)}$. The separation in the adhesive bond line continues to grow in the post-peak regime to 34% $P_{peak(post)}$.

Figure 6. Longitudinal strains measured by DIC

Figure 7. Transverse strains measured by DIC

DIC-measured strains along the span-wise direction, i.e., longitudinal strains and along the chord-wise direction, i.e., transverse strains are shown for the same eight load levels in Figure 6 and 7, respectively. In these strain contours, the red color represents tensile strains while the blue color represents compressive strains. These measurements provide detailed information on how the specimen behaves locally and they are essential for understanding the damage progress and the final failure. In particular, a few post-peak characteristics are worth noting:

- At 90% $P_{peak(post)}$: In Figure 6, longitudinal tensile strains shown in red appear to spread in two regions. The first region is close to the trailing edge line and it evolves from the tensile region at the previous load level 100% P_{peak}. The other region is just underneath the first region in the sandwich panel. The two regions merge into one at the following load steps. In Figure 7, transverse tensile strains shown in red at this load level locate at two curved bands running approximately in parallel with each other.
- At 47% $P_{peak(post)}$: In Figure 6, The longitudinal compressive strains at one side of the buckling wave near the trailing edge line are significantly decreased from the previous load level. This is caused by the change of load path when the trailing edge bond line is separated due to adhesive joint failure. The similar observation can be made in Figure 7 for the transverse tensile strains in the same region. The red region with high longitudinal tensile strains becomes narrower and grows towards the cutline as compressive deformation increases.
- At 34% $P_{peak(post)}$: With the increase of adhesive joint failure, both tensile and compressive strains are localized rapidly as shown in both Figure 6 and 7. In the meantime, the sandwich panel at the 21.45m section deforms more. The overall characteristics of strain distributions do not change significantly afterwards.

3.2 Post-test failure inspection

Thorough post-test failure inspection is carried out to examine failure modes and failure characteristics. As shown in Figure 8, a few types of failure modes are observed in the trailing edge region. With reference to ASTM D5573 [15], the trailing edge adhesive joint is found to exhibit cohesive failure and fiber-tear failure. The cohesive failure occurs within the adhesive material and the fiber-tear failure occurs exclusively within the matrix and is characterized by the appearance of fibers on both ruptured surfaces. To facilitate this observation, the specimen is cut and the ruptured surfaces are examined as shown in the figure. The skin laminates at the suction side, i.e., the side without DIC speckles, show laminate fracture and delamination. The skin laminates at the pressure side also show laminate fracture as shown in Figure 9. An infrared thermal image, Figure 9(c), is also shown here to better visualize the cracks. There is no delamination in these fractured skin laminates.

Figure 8. The post-test observation of trailing edge failures

(a) Trailing edge debonding; (b) Failure observed from the top side; (c) Failure observed from the suction side; (d) Failure observed after the specimen is cut; (e) Failure surface on the adhesive side; (f) Failure surface on the laminate side

Figure 9. The post-test observation of skin laminate fracture at the pressure side

In order to examine any internal damages that might be hidden from the view, destructive inspection is performed on the 21.45 m cross section as shown in Figure 10. Multiple failure modes present in the cross section and they include foam core material failure, skin/core debonding, delamination of trailing edge laminates, debonding of adhesive joint and skin laminate fracture.

Figure 10. Internal failure observed at the 21.45 m cross section after test

4. FE modeling

An FE model is developed in this study to complement comprehensive experimental investigation. The particular interest is placed on simulating the damage progress of different failure modes. By doing this, it is expected to obtain a more complete understanding on the failure sequence of the trailing edge section and the underlying mechanisms.

4.1 Modeling detailed geometry

Solid elements are used in the model in order to predict the failure modes associated with three-dimensional stresses and strains. An advantage of using solid elements is that the specimen's geometry can be modeled in detail at material and thickness transitions where local stresses and strains are critical for accurate prediction of material failures. The FE software Abaqus [16] is used to build the numerical model, where the element type C3D8R is used for composite materials and foam core materials, and the element type COH3D8 is used for the adhesive material. Figure 11 shows the FE model of the subcomponent of the trailing edge section. The detailed mesh of a cross section is shown in Figure 12. In the sandwich panels, three solid elements are used along the thickness direction representing two composite skin laminates and a foam core material. The typical mesh size is 25 x 25 x *t* mm and 25 x 10 x *t* mm for the solid elements at sandwich panels and at trailing edge regions, respectively, and *t* is the thickness of different materials. The mesh size is chosen based on previous simulation experience taking into account the element aspect ratio and the computational time. In total, there are approximately 70,500 solid elements in the model.

Figure 11. The FE model of the trailing edge section specimen

Figure 12. The detailed mesh of a cross section

4.2 Modeling boundary and load conditions

In the FE model as shown in Figure 11, plywood reinforcement and overlamination at specimen's boundaries are modeled as shell elements S4R. The test rig is not modeled due to its complexity. Instead, a practical modeling approach is used to simplify the load transfer system provided by the test rig. First, multiple point constraint (MPC) with rigid beams is applied to both ends of the specimen considering the internal plywood reinforcement as shown in Figure 1. Secondly, a local coordinate system is assigned to the reference nodes so that appropriate boundary constraints only allow the rotation of two end sections about the local y' axis, representing the hinge connections in the test setup. Thirdly, rigid body connections are used to model two steel loading plates in the test rig. Finally, a connector element is used to model the hydraulic actuator with a prescribed axial stroke, allowing the same forces to be transferred to two end sections. The simulation is run in displacement control and both the displacement and the force of the connector are monitored during the simulation.

Contact properties are assigned to two internal surfaces of sandwich panels. This is done due to the concern that the two surfaces might contact with each other considering the small distance in the tapering region near the trailing edge, e.g., the minimum distance $d \approx 4.2$ mm is found at the 21.45 m section as shown in Figure 12. The coefficient of friction is set to 0.3 in the FE analysis and it is assumed to be independent of the slip rate and the contact pressure.

4.3 Modeling material damages

In order to capture major failure modes and thereby predict the entire failure process of the subcomponent, three types of material damage are included in the model: Composite material failure, foam core failure and adhesive joint failure.

A damage-mechanics based progressive failure analysis approach is used to model composite material failure at a laminate level in a three-dimensional stress/strain state. In this approach, the Tsai-Wu failure criterion [17] is decomposed into a fiber-failure dominant mode and a matrix-failure dominant mode, and both are treated as in-plane composite failure. The stress based Yeh-Stratton criterion [18] is modified as proposed in [19] using three through-thickness strain components to determine the occurrence of delamination. Different elastic constants of materials are degraded to zero based on the specific failure mode determined by the failure criterion.

The PVC foam used in sandwich panels is modeled as a crushable material which deforms plastically beyond the linear elastic regime under compression due to cell wall buckling and as an elastic-plastic material under tension. The yield surface is a von Mises circle in the deviatoric stress plane and an ellipse in the meridional stress plane. Volumetric hardening is used to determine the evolution of the yield surface based on the volumetric compacting plastic strain experienced by the foam core material. Theoretical formulations of this model can be found in [20].

The cohesive zone model available in Abaqus [16] is used to predict the debonding of adhesive joints in the trailing edge. This study assumes that the failure of the adhesive material initiates once the quadratic nominal stress criterion is satisfied. Only the cohesion failure mode observed within the adhesive material is considered in the model. Stiffness degradation is activated after the failure initiation. The critical fracture energy is given by the Benzeggagh-Kenane fracture criterion [21]. Material properties of composites, PVC foams and adhesive used in the FE analysis are shown in Appendix.

4.4 Other information on FE analysis

The FE analysis is run in the DTU High Performance Computing (HPC) https://www.hpc.dtu.dk/ cluster Jess under Linux using 20 compute nodes. A user subroutine is developed to implement the progressive failure analysis approach. This modeling approach has been used in previous studies [19, 22] to predict composite failure of a full-scale blade. The Newton-Raphson method is used to perform nonlinear FE analysis in this study. The method has a quadratic convergence. Due to instabilities in the nonlinear analysis, which originate from buckling, material failure and the change of contact conditions, considerable difficulties in convergence may occur. A few analysis settings are used to improve the convergence. An artificial damping is added to the model by specifying a dissipated energy fraction of $2x10^{-4}$ to achieve adaptive automatic stabilization. The initial time increment is set to $5x10^{-5}$ out of the total time period of the step, i.e., 1, in the analysis. The minimum and maximum time increments are $1x10^{-9}$ and $1x10^{-2}$, respectively. The actual time increment is adjusted automatically between these two values depending on the convergence status during the analysis.

Figure 13. The comparison between the measured and the predicted global structural response

5. Numerical analysis and discussion

5.1 Predicted applied load vs. displacement response

The predicted global structural response in terms of applied loads and actuator displacement is plotted in Figure 13 together with experimental results. In general, the predicted curve follows the trend of the experimental curve in linear, buckling and post-peak regimes. However, both the buckling resistance and the peak load are overestimated. Several observations are worth noting:

- In the linear regime: there is only one slope, k=0.925, in the prediction, while there are two slopes, k=0.728 and 0.912, in the test. The increase of slopes observed in the test indicates the probable change of the initial contact conditions at the boundaries of the specimen. Small gaps between the specimen and the test rig and insufficient stiffness of the epoxy glue applied between the specimen and plywood clamps might have allowed the boundaries to deform. A change of boundary conditions is not possible in the numerical model as rigid beam constraints and rigid body connections are applied. The effect of the initial boundary conditions become less significant with the increase of the load level as structural behavior will dominate the global structural response. As shown in the figure,

the numerical model predicts the second slope observed in the test very well, which also justifies that the geometry and material stiffness of the specimen are modeled correctly.

- In the pre-peak nonlinear regime: both the buckling resistance and the peak load are overestimated. As discussed above, this is probably due to the change of initial boundary conditions in the test indicated by two slopes before the specimen buckles. Considering the rigid boundary conditions in the FE model, the overestimation is understandable. In order to have a generic model applicable for parametric study, this study did not make efforts to modify the boundary conditions in the numerical model to match those actually present in this particular test. Despite the discrepancy in load levels, the predicted curve of structural response follows the general trend of the experimental curve from the start of buckling deformation to the peak load. The specimen displacements at the start of buckling deformation and at the peak load are slightly overestimated compared to the experimental results.
- In the post-peak regime: although the predicted post-peak curve is quantitatively off from the experimental curve, the numerical model is able to predict the three significant step-wise drops of the applied load observed in the test. Considering the complexity of the structural response associated with multiple nonlinearities in the post-peak regime, the dominant post-peak response is considered to be captured reasonably well., As it can be seen in the following sections, this numerical model can provide very important information for understanding the failure process leading to the final failure modes and failure characteristics of the subcomponent. The simulation terminates when the applied loads begin to increase again, due to the numerical convergence problems associated with substantial material damages. It appears that the numerical simulation tries to follow the last part of the experimental curve when the load is increasing.

Figure 14. The comparison between the measured and the predicted displacement

5.2 Deformation field and strains field

The predicted out-of-plane deformation and strain distributions of the pressure side of the subcomponent are compared with the DIC measurements at 100% P_{peak} and 90% $P_{peak(post)}$. It can be seen from Figure 14 that the deformation distributions are predicted reasonably well. The numerical model captures the buckling waves along the trailing edge line and the 21.45 m section. When looking at strain distributions, which are usually more difficult to predict than deformation, the FE simulations show good agreement with the DIC measurements as shown in Figure 15 and 16. Notably, some local characteristics of strain distributions are captured by the numerical model, such as two regions with longitudinal tensile strains at the buckling wave as shown in red in Figure 15(d) and the curved band with transverse tensile strains near the trailing edge line as shown in red in Figure 16(b) and (d). The accurate prediction of these local strain characteristics is essential to the prediction of progressive failure of the trailing edge section during the loading.

Figure 15. The comparison between the measured and the predicted longitudinal strains

Figure 16. The comparison between the measured and the predicted transverse strains

5.3 Contact prediction

As one of other important factors in the failure process, the contact status of two inside surfaces of sandwich panels is presented. Figure 17 visualizes the distance between two inside surfaces that might contact during the loading. The sandwich panel at the pressure side is removed from the figure in order to present the contact region. The region highlighted in black represents the location where two surfaces contact with each other. It can be seen that the initial contact occurs at a very early stage when the global structural response is still linear during the loading. The initial contact locates around the region where the sandwich panels taper to the trailing edge at the 21.45 m section. With the increase of applied loads, the area of contact also increases. A new contact area appears and grows until the applied loads peak. In the post-peak regime, both contact areas evolve further due to the change of load path and the stress redistribution caused by different failures, which will be discussed in detail in the following section.

Figure 17. The contact status of two inside surfaces of sandwich panels
(The pressure side panel removed)

5.4 Failure prediction

5.4.1 Foam core failure

Figure 18 shows the progress of foam core failure at the 21.45 m section during the loading. Comparisons to experimental observations are also present in the figure. As indicated in the tapering region close to the trailing edge, the foam failure is present at the peak load. This finding also shows that the panel tapering could affect the peak load due to the thickness change of the foam core materials. In the post-peak regime, more significant foam failure occurs in the sandwich panel. The foam failure progresses away from the trailing edge and towards the specimen cutline with the increase of buckling deformation which also leads to the contact of two inside surfaces of sandwich panels. The predicted final foam core failure at two regions, i.e., region I and II, is compared to the experimental post-mortem observations. The numerical predictions show good capability of capturing the foam core failure in the sandwich panels.

Figure 18. The predicted progress of foam core failure at the 21.45 m section and the post-test observations

5.4.2 Adhesive joint failure

Figure 19 shows the quadratic nominal stress failure criterion (QUADSCRT) index of the cohesive elements. The value of 1 represents adhesive material failure. The figure visualizes the progress of adhesive failure during the loading. It can be seen that no adhesive failure occurs at the peak load. The initial adhesive joint failure starts in the post-peak regime when the buckling deformation of the trailing edge is well developed. This prediction also agrees with the experimental observation during the test. Notably, a new failure region appears at the load drop when δ/l_0 = 0.02 and progresses in the following load levels. The predicted locations of the final adhesive joint failure agree well with post-test observations as previously presented in Figure 8.

Figure 19. The predicted progress of adhesive failure at the trailing edge bondline

5.4.3 Composite failure

The predicted composite failure only occurs in the post-peak regime starting from 90% $P_{peak(post)}$. Matrix-dominant failure occurs before other types of failure, i.e., delamination and fiber-dominant failure. The final failure is located primarily in two regions. The first region is close to the trailing edge from 21.3 to 21.6 m section as shown in Figure 20; the other region is at the sandwich skins at the pressure side of the specimen as shown in Figure 21. Comparisons between the predicted final failure of composites and experimental post-mortem observations are also present in the figures.

Figure 20. The predicted final failure of composites close to the trailing edge and the post-test observations

Figure 21. The predicted final failure of composites at the sandwich skin and the post-test observations

The composite laminates close to the trailing edge show three types of failure modes, among which the matrix-dominant failure and delamination are more significant than the fiber-dominant failure. The failure region spreads longitudinally along the trailing edge line, which agrees well with experimental observations.

For the composite failure at the sandwich skins at the pressure side, the numerical model predicts the failure location and failure modes correctly. There is no delamination as observed in the test. It is noted that the minor matrix-dominant failure is also predicted close to the trailing edge, while no observation of such failure is found in the test. This might be due to the painted region that prevents clear inspections on the matrix cracks. In general, the numerical model shows good capability of capturing multiple failure modes and their typical characteristics observed in the subcomponent specimen.

6. Failure mechanisms of the trailing edge section

Based on comprehensive comparisons and good correlations between experimental results and numerical predictions, it is reasonable to use the developed FE model to complement experimental measurements, and the plausible underlying mechanisms of the trailing edge section can be investigated. Several important structural responses are present in the failure process as shown in Figure 22 and they are elaborated here:

Figure 22. The predicted structural responses of the trailing edge section

(1) Two sandwich panels of the trailing edge section start to contact with each other at the early stage of the loading. This is due to a small gap between two inside surfaces in the tapering region. The contact imposes additional constraints to the panels. The global structural response is still linear.

(2) With the increase of the applied load, two trailing edge sandwich panels start to exhibit buckling deformation. In the buckling regime, foam core materials start to yield due to increased deformation. The applied load reaches the peak thereafter.

(3) In the post-peak regime, adhesive materials in the trailing edge bond line starts to fail. The adhesive damage evolves during the entire post-peak period together with the change of contact status of two sandwich panels, the failure of foam core materials and the failure of composite materials.

(4) The failure of the composite materials starts in the post-peak regime after the initial failure of adhesive materials. The composite failure occurs first in the region close to the trailing edge in the form of the matrix-dominant mode, delamination and the fiber-dominant mode sequentially.

(5) The other region of composite failure is in the sandwich panel at the pressure side of the specimen. The composite failure occurs here after the failure near the trailing edge. The matrix-dominant failure develops before the fiber-dominant failure, while no delamination occurs in this region.

7. Conclusions and future study

This work presents a comprehensive study on the structural failure of a trailing edge section cut from a full-scale composite rotor blade. The entire failure sequence including the post-peak response is investigated through a thorough experimental study and detailed nonlinear FE analysis. Major findings of this work are:

- Using a continuum damage-mechanics based approach in a three-dimensional stress/strain state, the FE modeling techniques presented in this study show good capabilities to predict buckling deformation, strain distributions and the post-peak response that lead to multiple failure modes and failure characteristics of the trailing edge section.
- In addition to the well-known buckling-driven failure phenomenon, the contact between two inside surfaces of sandwich panels affects the buckling resistance and the ultimate strength, or the peak load, of the trailing edge sections. It is important to include contact properties of the trailing edge panels in the numerical model to capture the potential surface contact.

- Solid elements, rather than shell elements with offset thickness, should be used to better represent the actual thickness of trailing edge panels, which could facilitate more realistic and accurate prediction of trailing edge response as observed in this study.
- The foam core failure and the panel contact start before the peak load in the region close to the trailing edge. It is possible to increase the peak load of the trailing edge section by material tailoring and panel tapering in this local region.
- The failure of both composite materials and adhesive materials occurs in the post-peak regime. The matrix-dominant failure and delamination develop before the fiber-dominant failure in composite laminates in the trailing edge section.

In this study, only the critical load condition with the trailing edge section in compression is examined. The effect of load combinations on the failure of trailing edge sections should be further investigated. It is also of interest to examine the effect of different tapering on failure behavior of trailing edge sections of wind turbine blades. As the failure process is both specimen and load dependent, it should be noted that different blades with different material properties, geometric profiles and loading conditions could show different failure behavior. More parametric studies are necessary to generalize findings using the numerical method presented in this study.

Acknowledgements:

This study is partly funded by the European Commission's Seventh Framework Programme through the IRPWind project (grant agreement No. 609795). We would like to thank SSP Technology A/S for providing the wind turbine blade in this research. We also want to thank Mr. Federico Belloni for supporting data acquisition, Ms. Jing Tang for supporting geometric meshing and Dr. Philipp Ulrich Haselbach for technical discussion. We would like to thank anonymous reviewers for their valuable suggestions to this work.

Appendix:

Material properties of composites, PVC foams and adhesive used in the FE analysis are presented here. Most material properties are specified by the manufacturer and based on material tests. The material properties in the through-thickness direction are assumed. The material properties of overlamination by wet layup are assumed. The convention of three-dimensional stress/strain components in composite materials follows Figure A1 in the previous work [19].

Table A1. Elastic properties of composite materials

	E_{11} GPa	E_{22} GPa	E_{33} GPa	ν_{12} -	ν_{13} -	ν_{23} -	G_{12} GPa	G_{13} GPa	G_{23} GPa
Unidirectional laminate	41.26	11.39	11.39	0.33	0.33	0.21	3.91	3.91	3.91
Biaxial laminate_type#1	11.58	11.58	11.58	0.48	0.10	0.10	10.66	10.66	5.77
Biaxial laminate_type#2	12.75	12.75	12.75	0.48	0.10	0.10	10.06	10.66	6.35
Triaxial laminate_type#1	20.26	10.42	10.42	0.45	0.10	0.10	7.35	7.35	5.19
Triaxial laminate_type#2	16.70	8.59	8.59	0.45	0.10	0.10	6.61	6.61	4.28
Overlamination (wet layup)	18.21	18.21	18.21	0.48	0.10	0.10	14.37	15.23	9.07

Table A2. Strength properties of composite materials

	$\sigma_{11}^{u\_t}$ MPa	$\sigma_{11}^{u\_c}$ MPa	$\sigma_{22}^{u\_t}$ MPa	$\sigma_{22}^{u\_c}$ MPa	$\sigma_{33}^{u\_t}$ MPa	$\sigma_{33}^{u\_c}$ MPa	σ_{12}^{u} MPa	σ_{13}^{u} MPa	σ_{23}^{u} MPa
Unidirectional laminate	903.60	660.20	42.14	170.00	30.00	170.00	50.00	55.00	45.00
Biaxial laminate_type#1	123.90	156.30	156.30	156.30	105.00	105.00	143.90	89.20	57.70
Biaxial laminate_type#2	214.20	184.90	184.90	184.90	105.00	105.00	143.90	89.20	57.70
Triaxial laminate_type#1	472.06	324.16	127.12	127.12	105.00	105.00	99.25	89.20	57.70
Triaxial laminate_type#2	389.00	267.00	105.00	105.00	105.00	105.00	89.20	89.20	57.70
Overlamination (wet layup)	-	-	-	-	-	-	-	-	-

Table A3. Through-thickness ultimate strains of composite materials

	$\varepsilon_{33}^{u\_t}$ %	ε_{13}^{u} %	ε_{23}^{u} %
Unidirectional laminate	0.21	1.10	0.81
Biaxial laminate_type#1	1.22	1.22	1.35
Biaxial laminate_type#2	1.22	1.22	1.35
Triaxial laminate_type#1	1.22	1.22	1.35
Triaxial laminate_type#2	1.22	1.22	1.35
Overlamination (wet layup)	-	-	-

Table A4. Material properties of adhesive used in the trailing edge bondline

E MPa	ν -	σ_{33}^{u} MPa	σ_{13}^{u} MPa	σ_{23}^{u} MPa	G_{Ic} N/m	G_{IIc} N/m	G_{IIIc} N/m	η -
3000	0.38	42	40	40	1200	6000	6000	1.75

G_{Ic}, G_{IIc}, G_{IIIc} are the critical energy release rates for Mode I, II and III fracture, respectively. η is a material constant defined in the Benzeggagh-Kenane fracture criterion [21].

Table A5. Material properties of PVC foam

E MPa	ν -	σ_y MPa	ε_y %
48.5	0.4	1.4	2.89

σ_y, ε_y are the yielding stress and strain of PVC foam, respectively.

References:

[1] Haselbach PU, Branner K. Initiation of trailing edge failure in full-scale wind turbine blade test. Eng Fract Mech 2016;162:136–54.

[2] Chen X., Experimental investigation on structural collapse of a large composite wind turbine blade under combined bending and torsion, Composite Structures, Volume 160, 15 January 2017, Pages 435–445.

[3] Chen X, Qin ZW, Yang K, Zhao XL, Xu JZ, Numerical analysis and experimental investigation of wind turbine blades with innovative features: Structural response and characteristics, Science China Technological Sciences, Volume 58, Issue 1, January 2015, Pages 1-8.

[4] M.A. Eder, K. Branner, P. Berring, F. Belloni, H. Stensgaard Toft, J.D. Sørensen, A. Corre, T.Lindby, A. Quispitup, and T.K. Petersen. Experimental Blade Research - phase 2. DTU Wind Energy. 108 p., report no. E-0083, 2015.

[5] Haselbach PU, Eder MA, Belloni F., A comprehensive investigation of trailing edge damage in a wind turbine rotor blade, Wind Energy, 2016. 19:1871–1888.

[6] Sayer F, Antoniou A, Van Wingerde A. Investigation of structural bond lines in wind turbine blades by sub-component tests. Int J Adhes Adhes 2012;37:129–35.

[7] Tang J, Chen X, Experimental investigation on ultimate strength and failure response of composite box beams used in wind turbine blades, Composite Structures, 198, pages: 19-34, 2018.

[8] Rosemeier M., Basters G., Antoniou A. Benefits of subcomponent over full-scale blade testing elaborated on a trailing-edge bond line design validation. Wind Energy Science. 2018;3(1):163–172.

[9] Rosemeier M., Antoniou A., Chen X., Lahuerta F., Berring P., Branner K., Trailing edge sub-component testing for wind turbine blades - Part A: Comparison of concepts. Wind Energy. To appear.

[10] Branner, K, Berring, P & Haselbach, PU 2016, 'Subcomponent testing of trailing edge panels in wind turbine blades'. in Proceedings of 17th European Conference on Composite Materials, Munich, Germany.

[11] Lahuerta F., Koorn N, Smissaert D., Wind turbine blade trailing edge failure assessment with sub-component test on static and fatigue load conditions, Composite Structures, 204 (2018) 755-766.

[12] DNV GL AS. Rotor blades for wind turbines. Standard, DNVGL-ST-0376, Edition December 2015.

[13] Pansart S. A new rotor blade standard for high product quality and flexible certification. Poster, EWEA 2015, European Wind Energy Association (EWEA), 17 - 20 November 2015, Paris, France.

[14] Antoniou A, Rosemeier M, Pueyo C, Makris A, Roukis G, Lahuerta F, et al. Testing report on blade subcomponents. Work Package 7.1: Efficient blade structure Deliverable number 7.1.2, Tech. rep., IRPWind, Grant agreement no 609795; 2017.

[15] ASTM International, ASTM D5573-99(2012), Standard practice for classifying failure modes in fiber-reinforced-plastic (FRP) joints, October 2012.

[16] Dassault Systemes Simulia Corp. ABAQUS/Standard User's Manual, Version 6.17, Dassault Systemes: Providence, RI, USA, 2017.

[17] Tsai, S. W. and Wu, E. M. A general theory of strength for anisotropic materials. Journal of Composite Materials. 1971. vol. 5, pp. 58–80.

[18] Yeh, H.Y. and Kim, C.H. The Yeh–Stratton criterion for composite materials, J Compos Mater, 1994, 28 1994, pp. 926-939.

[19] Chen X, Zhao XL, Xu JZ, Revisiting the structural collapse of a 52.3 m composite wind turbine blade in a full-scale bending test, Wind Energy, vol: 20, issue: 6, pages: 1111-1127, 2017.

[20] Deshpande, V.S., and N.A. Fleck, Isotropic Constitutive Model for Metallic Foams, Journal of the Mechanics and Physics of Solids, vol. 48, pp. 1253–1276, 2000.

[21] Benzeggagh, M. L., and M. Kenane, Measurement of Mixed-Mode Delamination Fracture Toughness of Unidirectional Glass/Epoxy Composites with Mixed-Mode Bending Apparatus, Composites Science and Technology, vol. 56, pp. 439–449, 1996.

[22] Chen X., Zhao W., Zhao XL, Xu JZ, Failure test and finite element simulation of a large wind turbine composite blade under static loading. Energies. Volume 7, Issue 4, 2014, Pages 2274-2297.

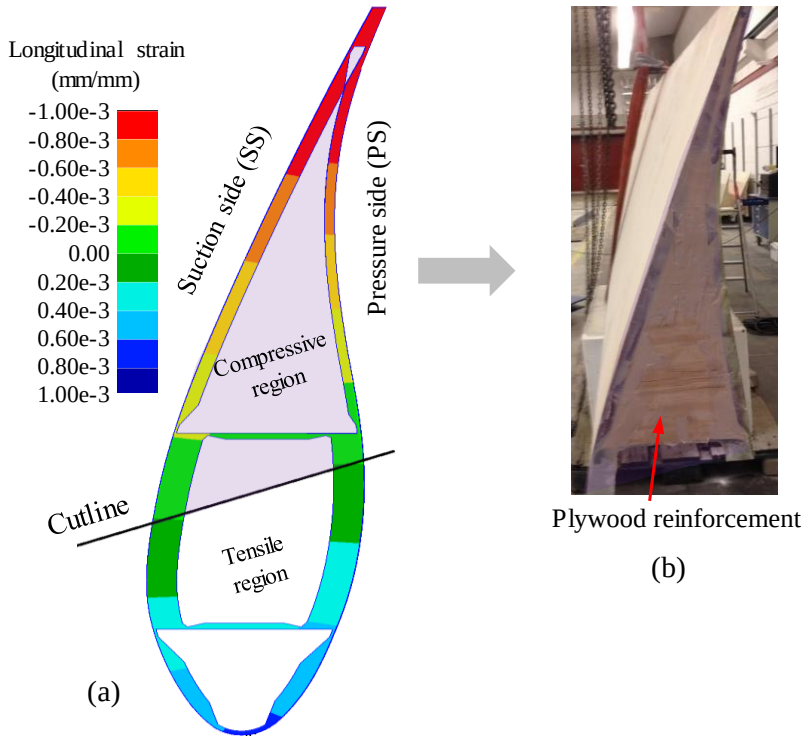

Figure 1. The subcomponent of a trailing edge section used in this study

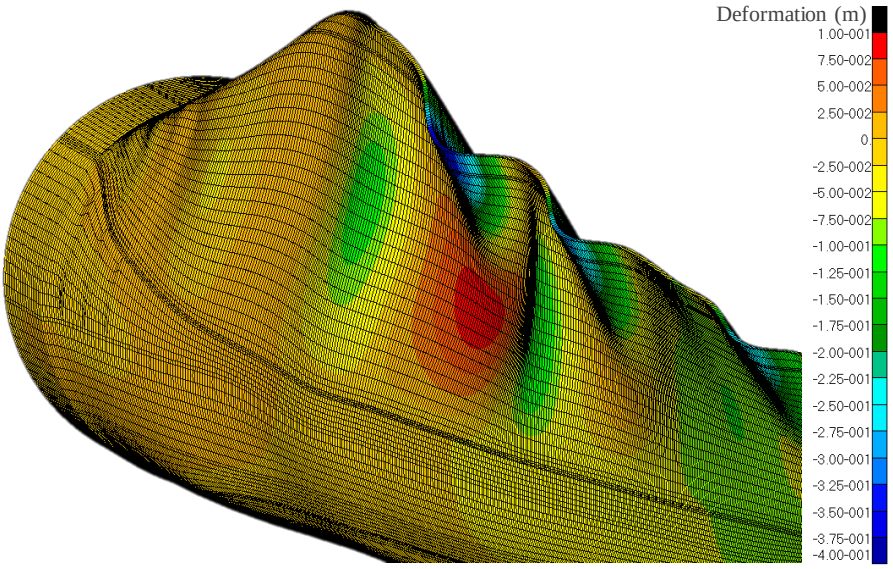

Figure 2. Trailing edge buckling of a full-scale blade under edgewise bending

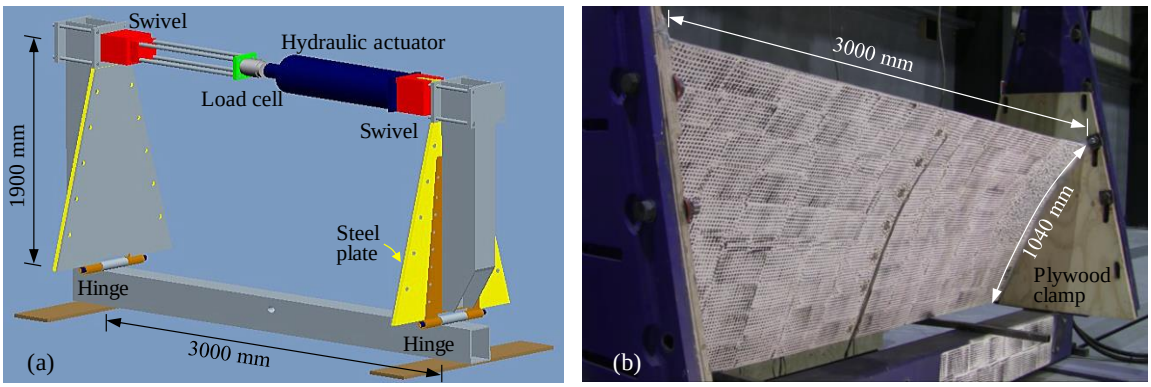

Figure 3. Subcomponent test setup

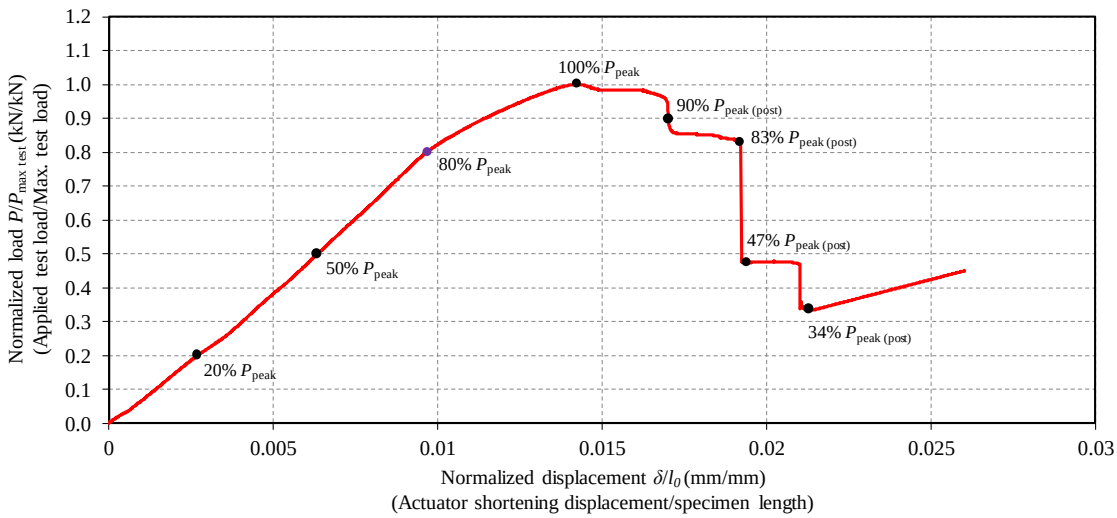

Figure 4. The global structural response of the trailing edge section

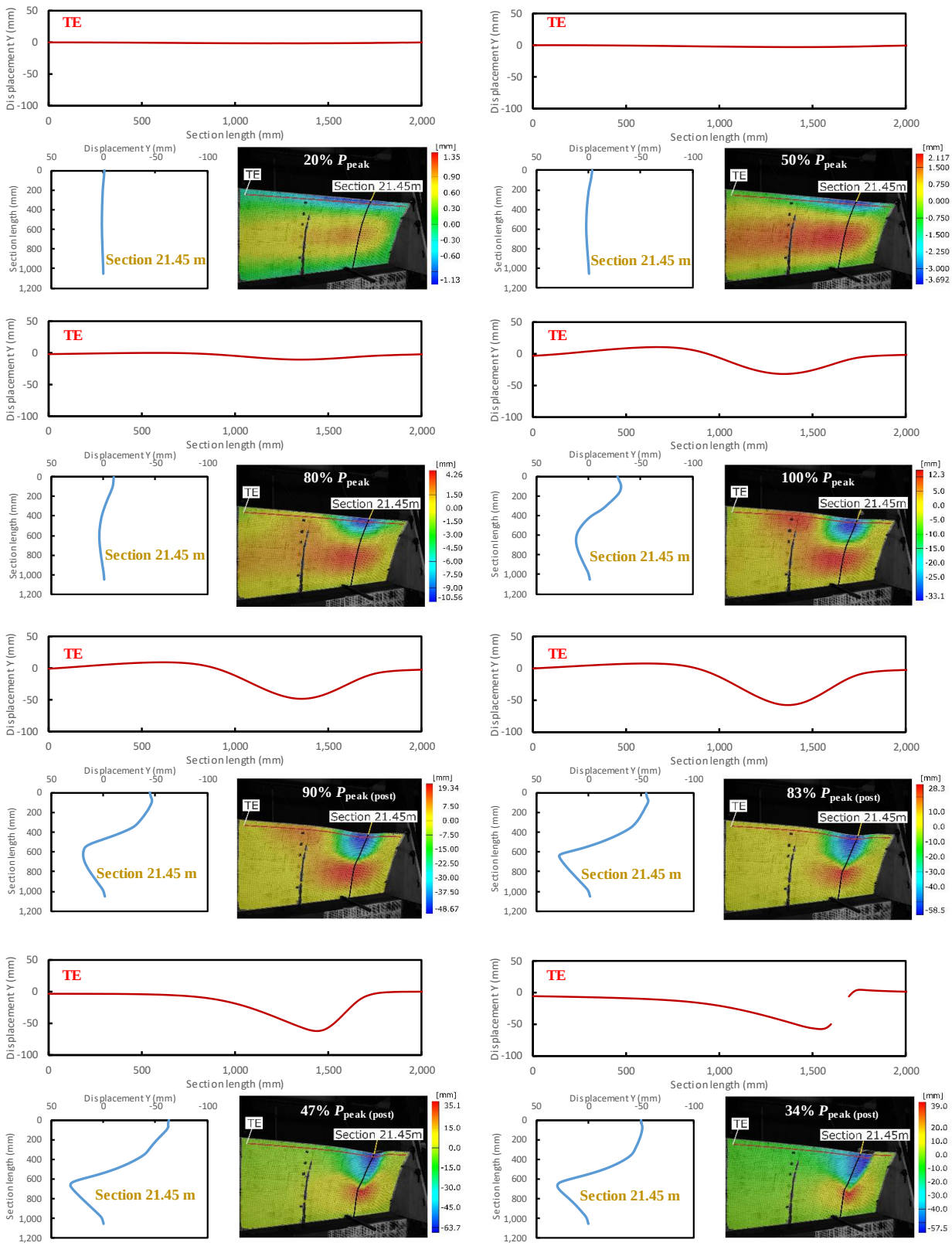

Figure 5. The out-of-plane deformation of the trailing edge section measured by DIC

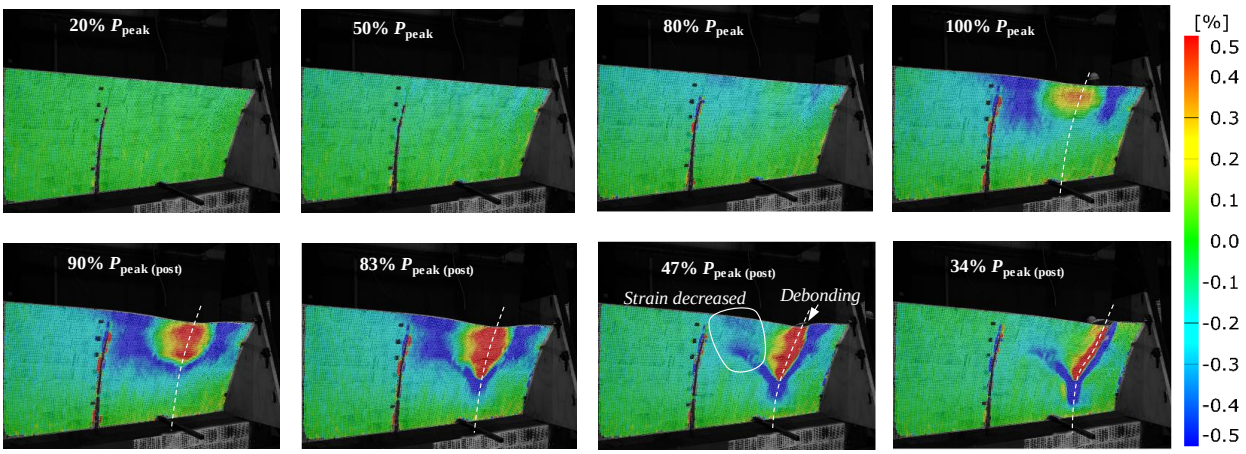

Figure 6. Longitudinal strains measured by DIC

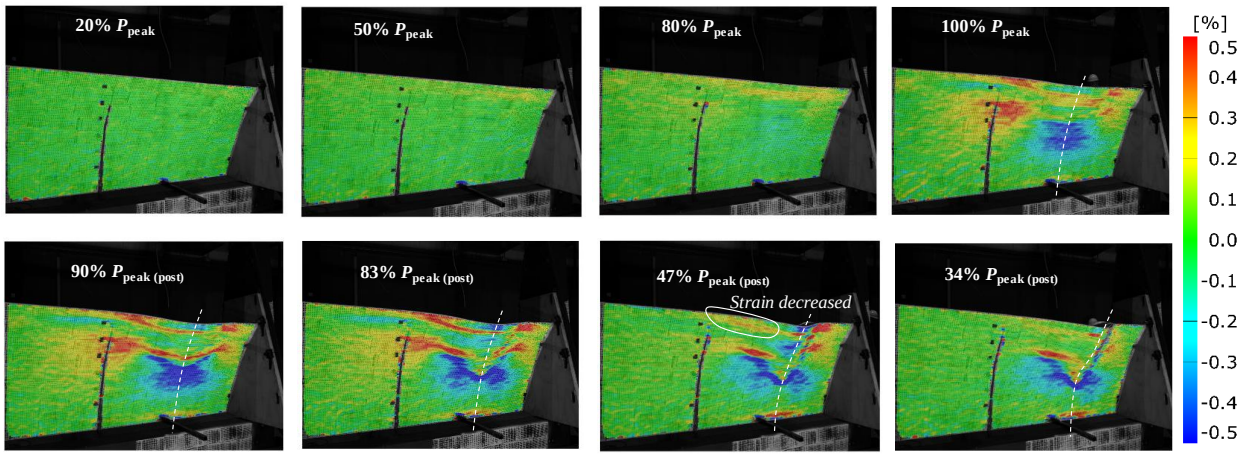

Figure 7. Transverse strains measured by DIC

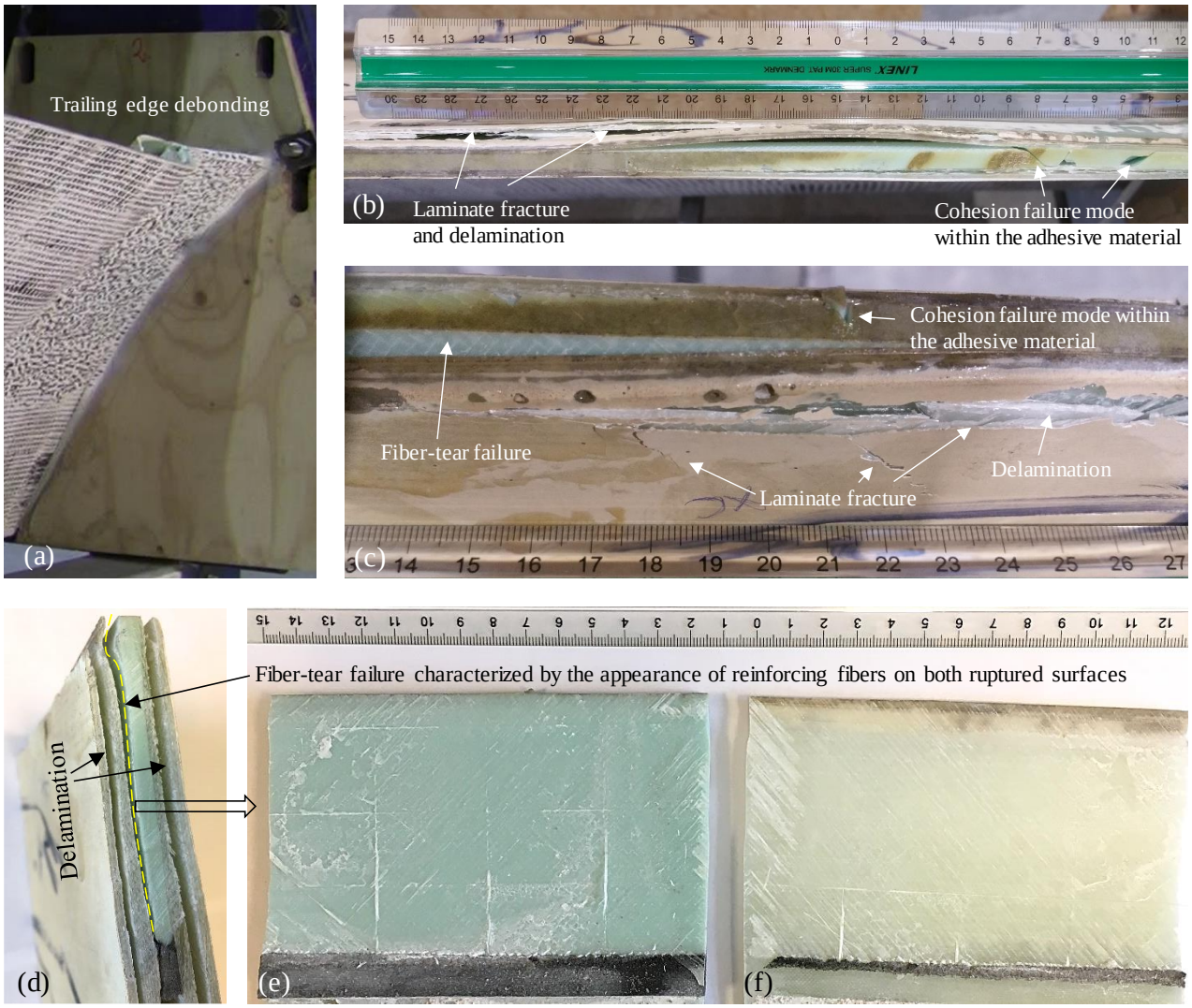

Figure 8. The post-test observation of trailing edge failures
(a) Trailing edge debonding; (b) Failure observed from the top side; (c) Failure observed from the suction side; (d) Failure observed after the specimen is cut; (e) Failure surface on the adhesive side; (f) Failure surface on the laminate side

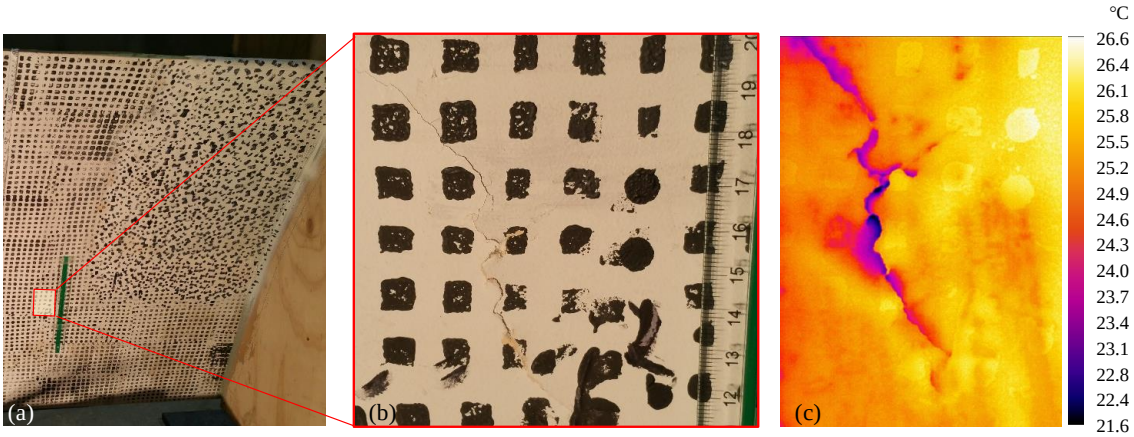

Figure 9. The post-test observation of skin laminate fracture at the pressure side

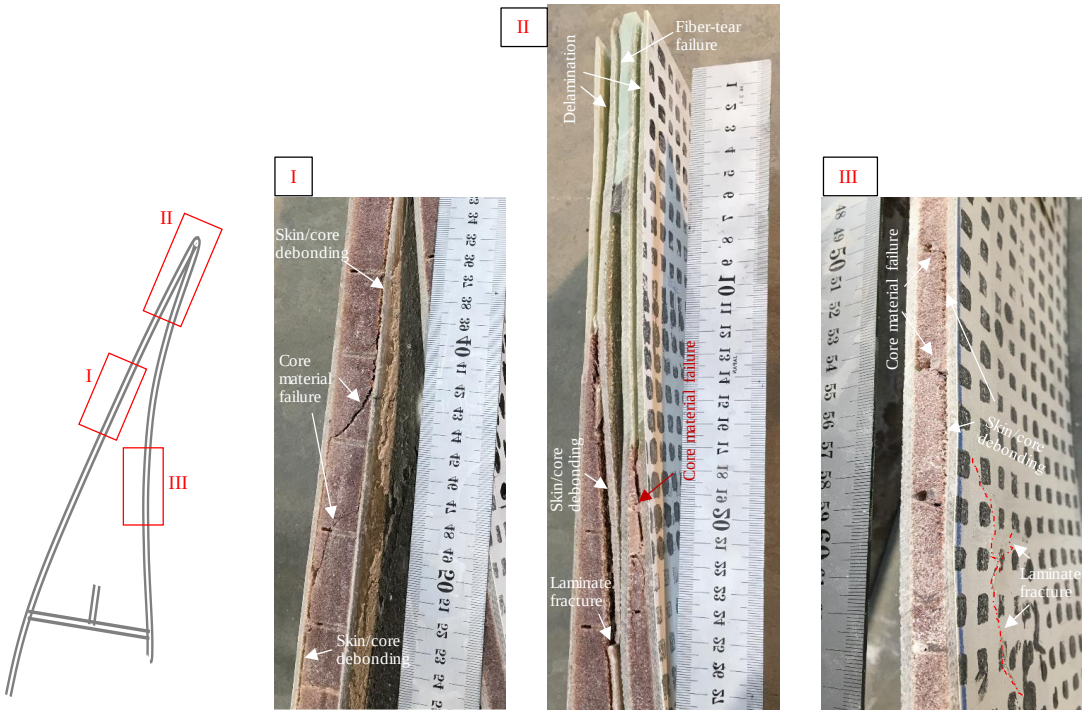

Figure 10. Internal failure observed at the 21.45 m cross section after test

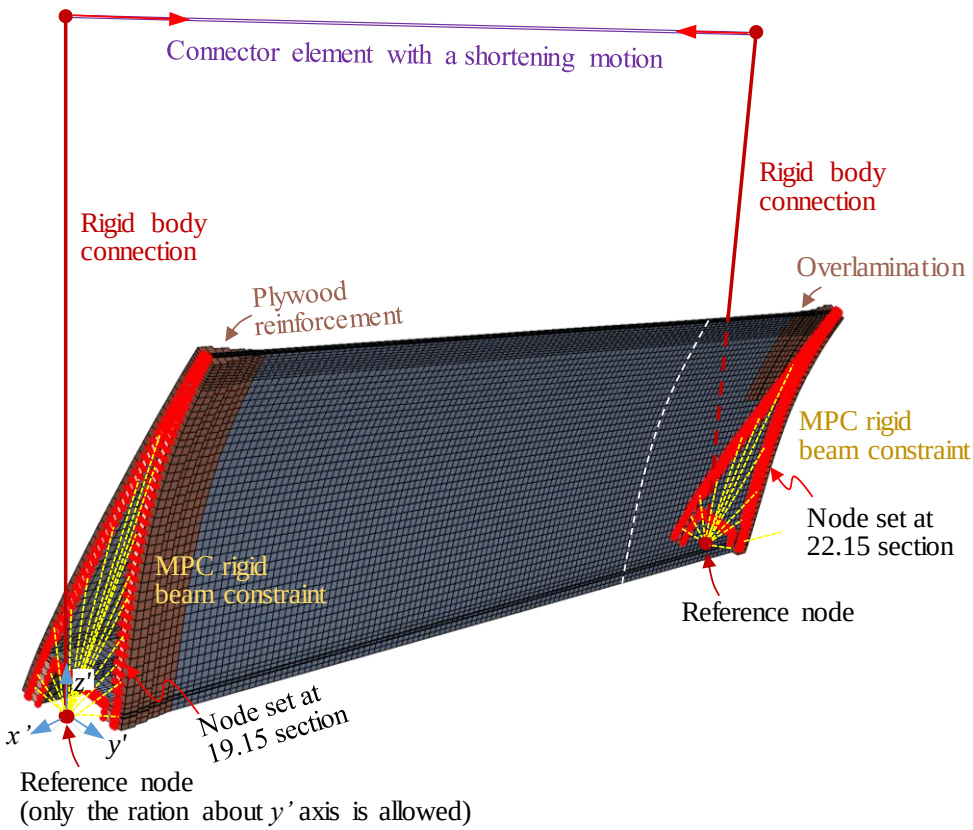

Figure 11. The FE model of the trailing edge section specimen

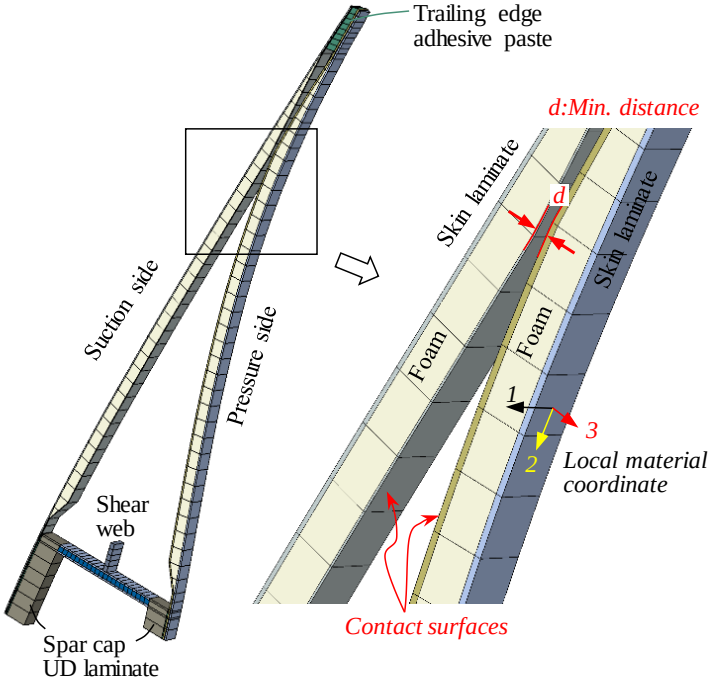

Figure 12. The detailed mesh of a cross section

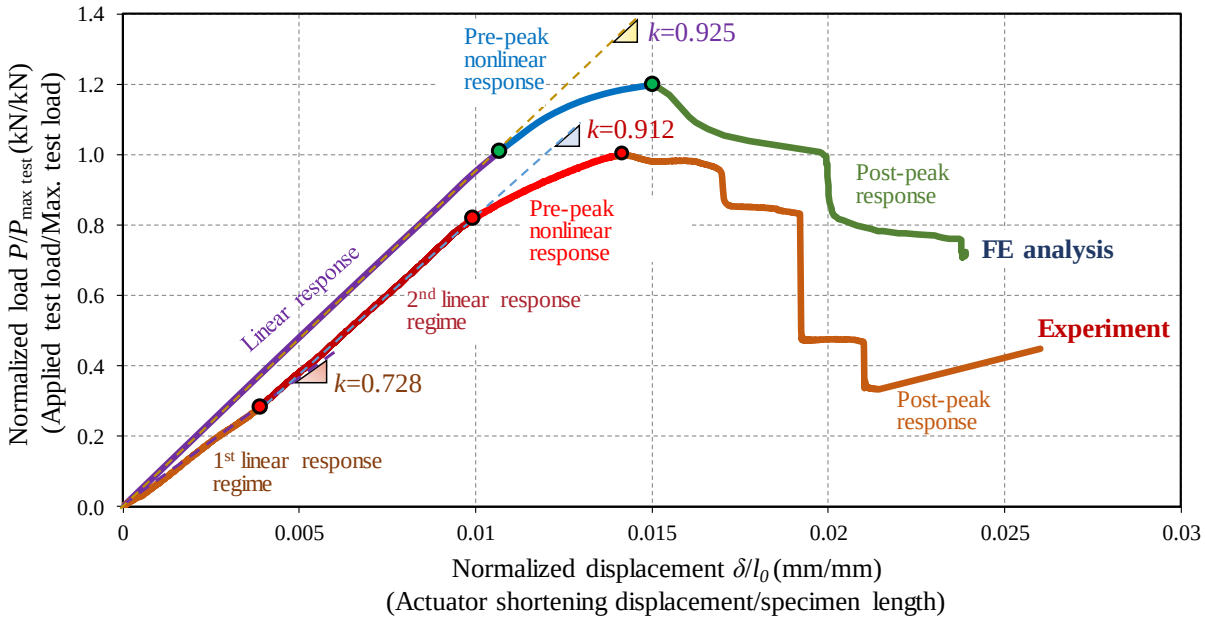

Figure 13. The comparison between the measured and the predicted global structural response

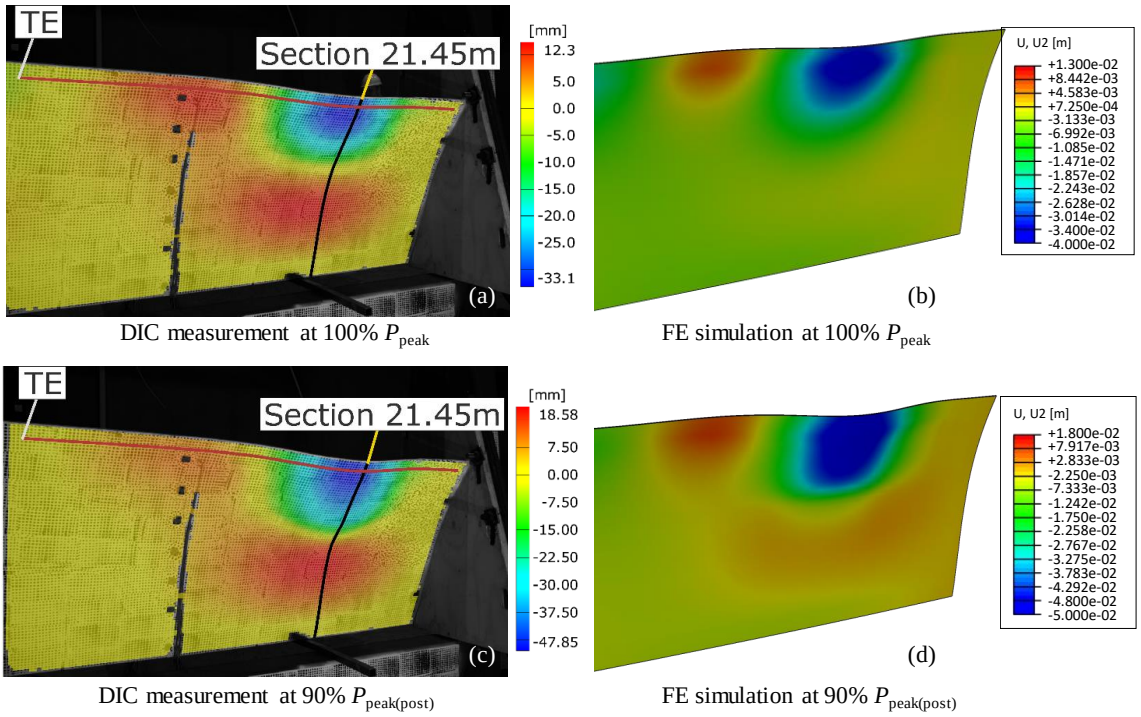

DIC measurement at 100% P_{peak} FE simulation at 100% P_{peak}

DIC measurement at 90% $P_{peak(post)}$ FE simulation at 90% $P_{peak(post)}$

Figure 14. The comparison between the measured and the predicted displacement

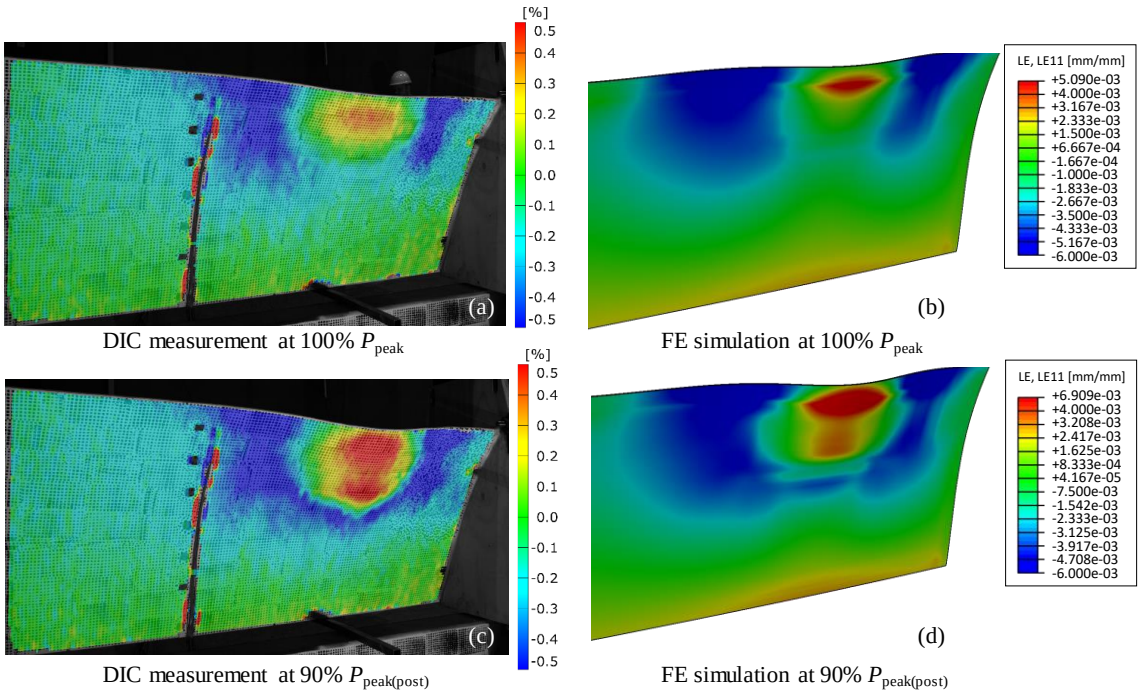

Figure 15. The comparison between the measured and the predicted longitudinal strains

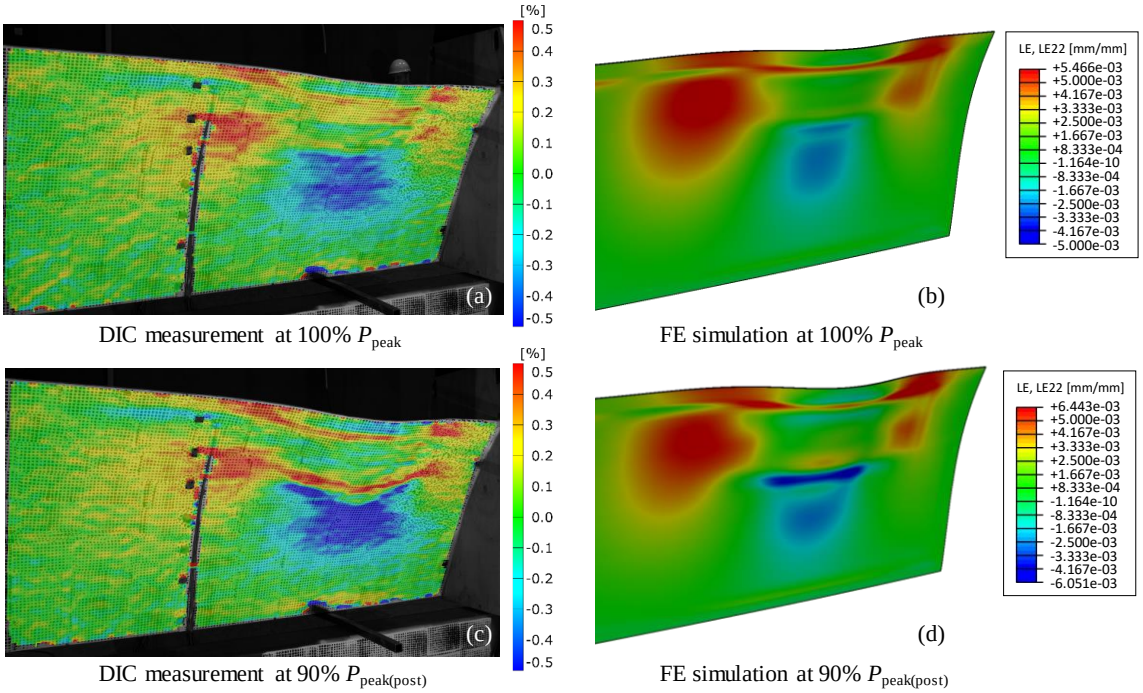

Figure 16. The comparison between the measured and the predicted transverse strains

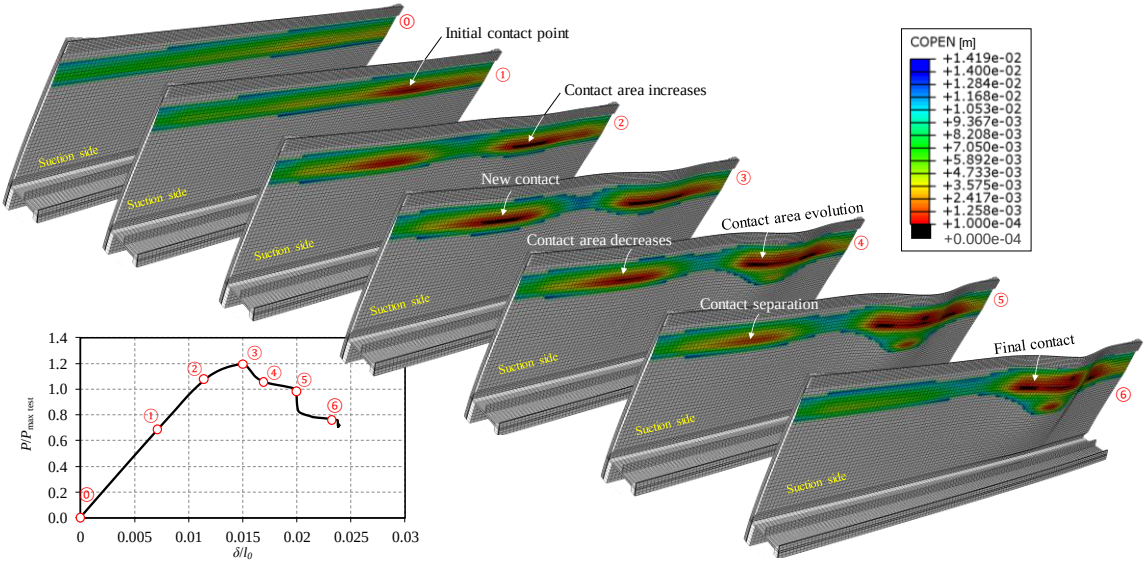

Figure 17. The contact status of two inside surfaces of sandwich panels (the pressure side panel removed)

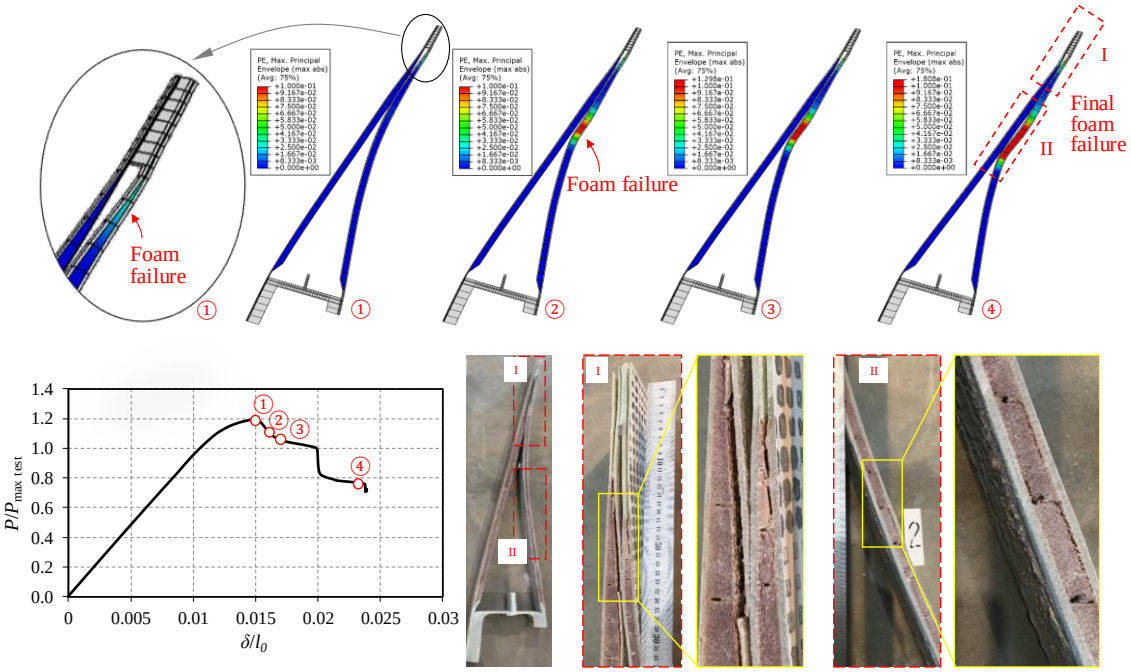

Figure 18. The predicted progress of foam core failure at the 21.45 m section and the post-test observations

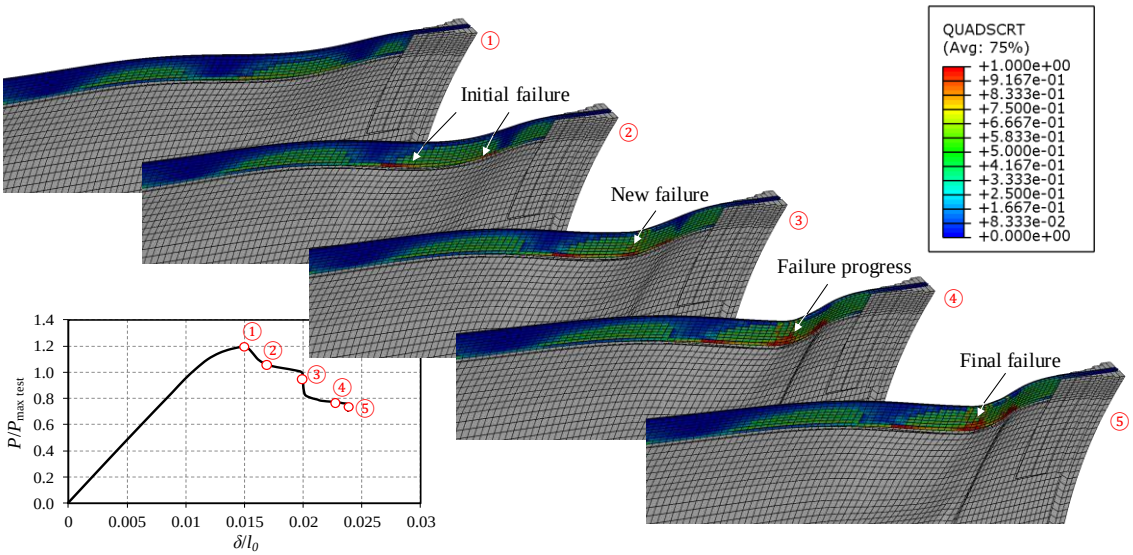

Figure 19. The predicted progress of adhesive failure at the trailing edge bondline

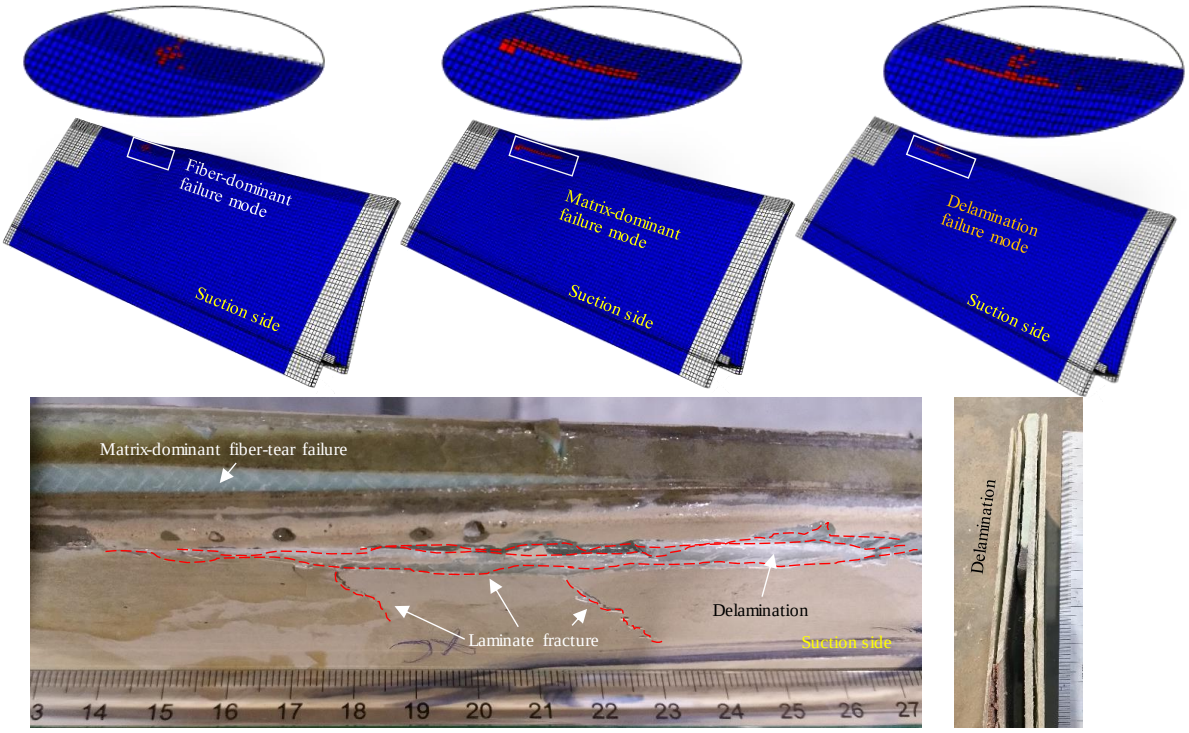

Figure 20. The predicted final failure of composites close to the trailing edge and the post-test observations

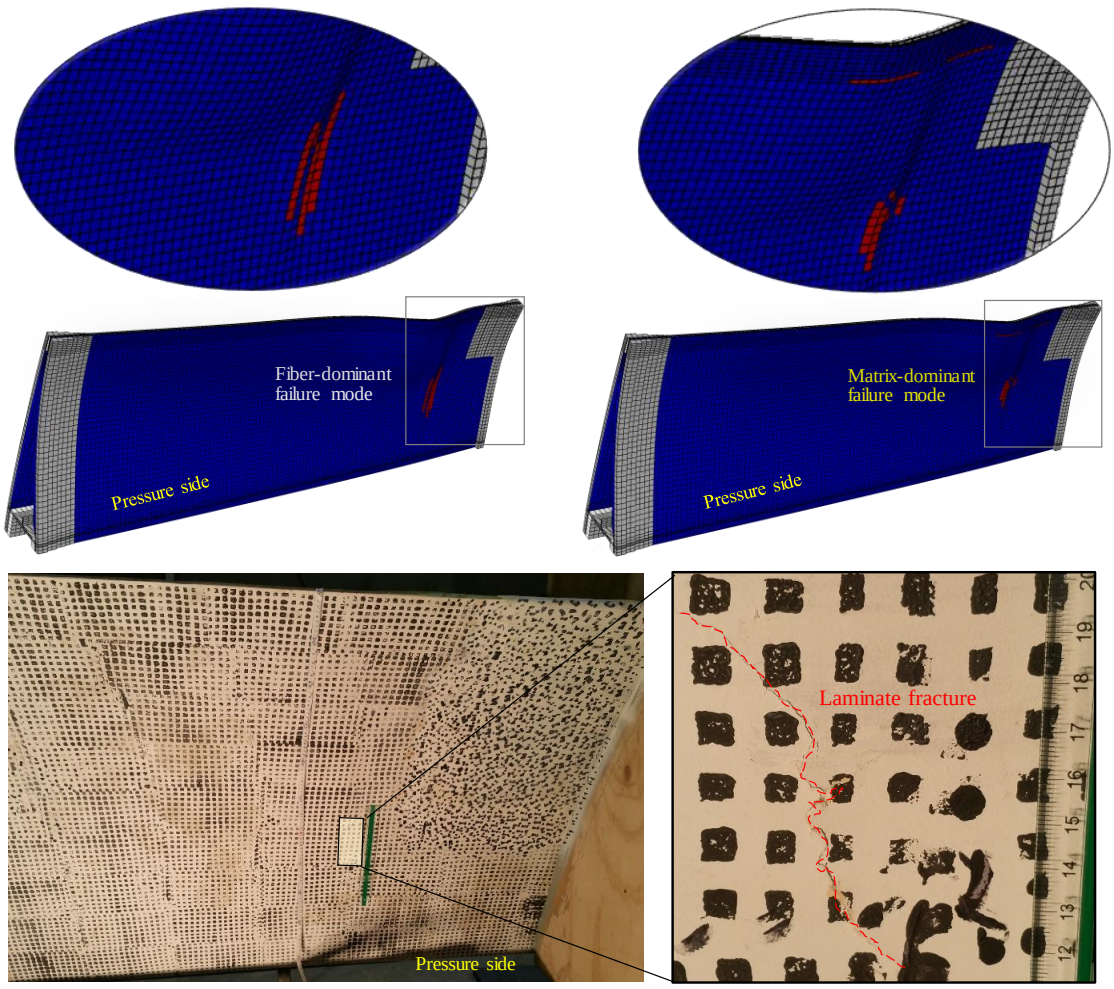

Figure 21. The predicted final failure of composites at the sandwich skin and the post-test observations

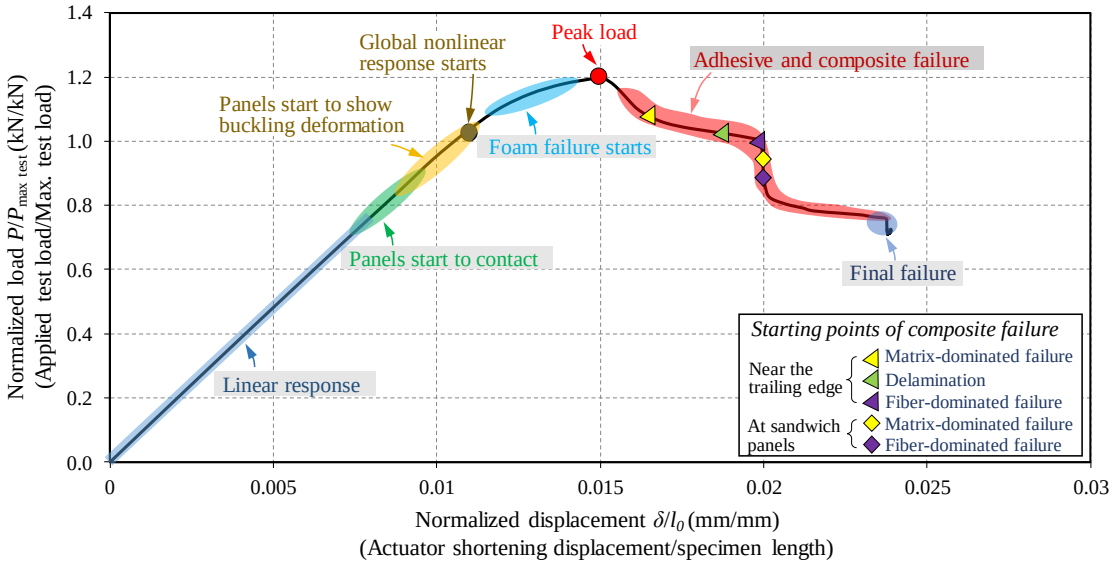

Figure 22. The predicted structural responses of the trailing edge section